










RESEARCH ARTICLE | APRIL 26 2023

# Chemical phases in the solution-grown Zn(O,S) buffer of post-annealed Cu(In,Ga)Se<sub>2</sub> solar cells investigated by transmission electron microscopy and electroreflectance

Xiaowei Jin ; Reinhard Schneider; Radian Popescu ; Jasmin Seeger ; Jonas Grutke ; Benedikt Zerulla ; Michael Hetterich ; Dimitrios Hariskos ; Wolfram Witte ; Michael Powalla; Dagmar Gerthsen 

 Check for updates

*J. Appl. Phys.* 133, 165303 (2023)

<https://doi.org/10.1063/5.0139264>



View Online



Export Citation

CrossMark

## Articles You May Be Interested In

Defect microchemistry in SiO<sub>2</sub>/Si structures

*Journal of Vacuum Science & Technology A* (May 1990)

Monte Carlo analysis of transient electron transport in wurtzite Zn<sub>1-x</sub>Mg<sub>x</sub>O combined with first principles calculations

*AIP Advances* (January 2015)

Effect of retrogression duration on the grain boundary microstructure and microchemistry of AA7010

*AIP Conference Proceedings* (April 2018)

500 kHz or 8.5 GHz?  
And all the ranges in between.

Lock-in Amplifiers for your periodic signal measurements



Find out more

 Zurich Instruments

# Chemical phases in the solution-grown Zn(O,S) buffer of post-annealed Cu(In,Ga)Se<sub>2</sub> solar cells investigated by transmission electron microscopy and electroreflectance

Cite as: J. Appl. Phys. **133**, 165303 (2023); doi: [10.1063/5.0139264](https://doi.org/10.1063/5.0139264)

Submitted: 19 December 2022 · Accepted: 8 April 2023 ·

Published Online: 26 April 2023



View Online



Export Citation



CrossMark

Xiaowei Jin,<sup>1,a)</sup> Reinhard Schneider,<sup>1</sup> Radian Popescu,<sup>1</sup> Jasmin Seeger,<sup>2</sup> Jonas Grutke,<sup>2</sup> Benedikt Zerulla,<sup>2</sup> Michael Hetterich,<sup>2,3</sup> Dimitrios Hariskos,<sup>4</sup> Wolfram Witte,<sup>4</sup> Michael Powalla,<sup>4</sup> and Dagmar Gerthsen<sup>1</sup>

## AFFILIATIONS

<sup>1</sup>Laboratorium für Elektronenmikroskopie, Karlsruher Institut für Technologie (KIT), Karlsruhe 76131, Germany

<sup>2</sup>Institut für Angewandte Physik, KIT, Karlsruhe 76131, Germany

<sup>3</sup>Lichttechnisches Institut, KIT, Karlsruhe 76131, Germany

<sup>4</sup>Zentrum für Sonnenenergie- und Wasserstoff-Forschung Baden-Württemberg (ZSW), Stuttgart 70563, Germany

<sup>a)</sup>Author to whom correspondence should be addressed: [xiaowei.jin@kit.edu](mailto:xiaowei.jin@kit.edu)

## ABSTRACT

Thin-film solar cells with Cu(In,Ga)Se<sub>2</sub> (CIGS) absorber layers have been intensively studied due to their high power conversion efficiencies. CIGS solar cells with Zn(O,S) buffer layers achieved record efficiencies due to their reduced parasitic absorption compared with the more commonly used CdS buffer. Accordingly, we have studied solution-grown Zn(O,S) buffer layers on polycrystalline CIGS absorber layers by complementary techniques. A bandgap energy  $E_g$  of 2.9 eV is detected by means of angle-resolved electroreflectance spectroscopy corresponding to Zn(O,S), whereas an additional  $E_g$  of 2.3 eV clearly appeared for a post-annealed CIGS solar cell (250 °C in air) compared with the as-grown state. To identify the chemical phase that contributes to the  $E_g$  of 2.3 eV, the microstructure and microchemistry of the Zn(O,S) buffer layers in the as-grown state and after annealing were analyzed by different transmission electron microscopic techniques on the submicrometer scale and energy-dispersive x-ray spectroscopy. We demonstrate that the combination of these methods facilitates a comprehensive analysis of the complex phase constitution of nanoscaled buffer layers. The results show that after annealing, the Cu concentration in Zn(O,S) is increased. This observation indicates the existence of an additional Cu-containing phase with  $E_g$  close to 2.3 eV, such as Cu<sub>2</sub>Se (2.23 eV) or CuS (2.36 eV), which could be one possible origin of the low power conversion efficiency and low fill factor of the solar cell under investigation.

© 2023 Author(s). All article content, except where otherwise noted, is licensed under a Creative Commons Attribution (CC BY) license (<http://creativecommons.org/licenses/by/4.0/>). <https://doi.org/10.1063/5.0139264>

## INTRODUCTION

Thin-film solar cells based on polycrystalline Cu(In,Ga)Se<sub>2</sub> (CIGS) absorbers have attracted much attention in recent years due to their high power conversion efficiency above 23%,<sup>1</sup> reduced energy, and material consumption compared with single-crystalline Si cells.<sup>2,3</sup> CIGS solar cells are often deposited on a soda-lime glass substrate and contain a Mo back contact, a CIGS absorber, a CdS

buffer layer, and an i-ZnO/ZnO:Al window layer.<sup>4,5</sup> In this case, the toxic CdS buffer layer with a bandgap energy  $E_g = 2.4\text{--}2.5$  eV<sup>6</sup> limits the cell performance due to parasitic absorption in the blue wavelength region. Thus, Cd-free buffer materials with larger  $E_g$  are expected to improve the solar-cell performance, among which Zn(O,S) has become a promising candidate due to its non-toxicity, wide and tunable  $E_g$  of 2.6–3.6 eV, earth abundance, and low cost.<sup>7,8</sup> Up to now, various techniques have been applied to deposit

Zn(O,S) layers on CIGS, e.g., sputtering,<sup>9,10</sup> atomic layer deposition,<sup>11</sup> chemical-bath deposition (CBD),<sup>12</sup> and electron-beam evaporation.<sup>13</sup> Among these, cells with CBD-Zn(O,S) buffer layers have shown the highest efficiencies and resulted in the current record CIGS device with 23.35%.<sup>1</sup>

The  $E_g$  of these very thin CBD-Zn(O,S) buffer layers with thicknesses in the range of 20–30 nm could be measured in complete CIGS devices with front and back contact by means of (averaged) angle-resolved electroreflectance spectroscopy (ARER).<sup>14,15</sup> As discussed below, in Zn(O,S) layers post-annealed at 250 °C in air, which is relatively high for such procedures, an unexpected  $E_g$  of 2.3 eV was clearly detected in addition to the  $E_g$  of Zn(O,S) at around 2.9 eV, indicating the formation of an additional phase that could be responsible for the very low power conversion efficiency. In general, post-annealing procedures at more moderate temperatures below 250 °C of complete CIGS devices with CBD-Zn(O,S) buffers are common measures to increase efficiency further.<sup>16–19</sup> However, also in these structures, a weak additional resonance at around 2.3 eV can be observed in ARER. To identify this additional phase, (scanning) transmission electron microscopy [(S)TEM], combined with energy-dispersive x-ray spectroscopy (EDXS) and nanobeam electron diffraction (NBED), was used to investigate the microstructural and microchemical properties of the as-grown and post-annealed solar cells, focusing on the CBD-Zn(O,S) buffer layers and the CIGS/Zn(O,S) interfacial regions. After annealing, the phase constitution of the Zn(O,S) buffer layer changes significantly on the nanoscale, which can be correlated with the extra signal in the ARER spectrum. Our work demonstrates that the chosen combination of complementary characterization techniques is well-suited to correlate physical properties like  $E_g$  with structural properties and microchemistry, which is essential to identify the chemical phases in CIGS devices on the submicrometer scale.

## EXPERIMENTAL

The CIGS solar cell studied in this work was fabricated on a soda–lime glass substrate with a sputtered Mo back contact. The p-type CIGS absorber was deposited by an in-line multi-stage co-evaporation process<sup>20</sup> with a nominal stoichiometry of  $\text{CuIn}_{0.7}\text{Ga}_{0.3}\text{Se}_2$  (i.e., 23 at.% Cu, 18 at.% In, 8 at.% Ga, and 51 at.% Se), as confirmed by x-ray fluorescence measurements.<sup>21</sup> The Zn(O,S) buffer layer was grown by CBD at 80 °C with a thickness of about 20 nm, which was performed in an ammonia solution with pH  $\sim$ 11 by the reaction of  $\text{ZnSO}_4$  with thiourea as

organosulfide.<sup>22</sup> The subsequent (Zn,Mg)O high-resistive layer was deposited by rf-sputtering and the front ZnO:Al contact layer by dc-sputtering. In addition, reference cells with CBD-CdS and i-ZnO as highly resistive layers were prepared for comparison. Table I provides an overview of the relevant samples with corresponding solar-cell parameters as measured under standard testing conditions from this CIGS deposition campaign. The CIGS solar cells with CdS and Zn(O,S) buffers exhibit good efficiencies on a 16%–17% level (see “sister samples”). Nevertheless, there are also some Zn(O,S)-buffered samples with a poor efficiency of around 7%, mainly as a result of a low fill factor due to the presence of a barrier at the absorber/buffer interface and combined with a shunting and reduced open-circuit voltage. One of these cells was chosen for the present detailed ARER/TEM analysis to shed more light on the poor device performance and possible origins. This complete CIGS solar cell with 7% efficiency was analyzed in the as-grown state and after post-annealing in air on a hot plate at a temperature of 250 °C (30 min), resulting in an almost dead cell with an efficiency below 2% due to severe shunting. We used this untypically high annealing temperature to further enhance the presence of the additional phase for the ARER/TEM studies.

The bandgap energies in the space charge region of the as-grown and annealed solar cells, respectively, were measured by ARER. This technique is based on acquiring a set of electroreflectance spectra in different specular reflection configurations, i.e., for various incidence and corresponding reflection angles. The resulting spectra are then transformed into peak-shaped modulus spectra and finally averaged in order to minimize line shape distortions due to interference effects. Further details can be found in Refs. 14 and 15.

Cross-sectional TEM samples of the as-grown and annealed solar cells were prepared by employing focused-ion beam (FIB) milling with a Thermo Fisher dual-beam Helios G4 FX microscope. The FIB lamellae were mounted on Si lift-out grids. We note that it is important to avoid Cu lift-out grids because stray x rays will induce large errors in the composition quantification of CIGS by EDXS. High-angle annular dark-field (HAADF) STEM imaging was performed on a FEI Tecnai Osiris microscope operated at 200 kV. The instrument is equipped with a high-brightness field-emission electron gun and a SuperX energy-dispersive x-ray detector system comprising four Si drift detectors. Recording and quantification of EDXS data were carried out by using the Bruker Esprit software version 2.1.

Quantitative EDXS data analysis with the Cliff-Lorimer thin-film approximation<sup>23</sup> is not sufficient because the absorption of soft

**TABLE I.** Solar-cell parameters power conversion efficiency  $\eta$ , open-circuit voltage  $V_{OC}$ , fill factor FF, and short-circuit current density  $j_{SC}$  for good CdS- and Zn(O,S)-buffered sister samples and a poor-performing CIGS sample with a CBD-Zn(O,S) buffer for ARER and TEM investigations.

Sample	Sister sample	Sister sample	ARER/TEM	ARER/TEM
Buffer system	CdS/i-ZnO	Zn(O,S)/Zn <sub>0.75</sub> Mg <sub>0.25</sub> O	Zn(O,S)/Zn <sub>0.75</sub> Mg <sub>0.25</sub> O	Zn(O,S)/Zn <sub>0.75</sub> Mg <sub>0.25</sub> O
State before $I$ – $V$	As grown	As grown	As grown	Anneal 250 °C
$\eta$ (%)	16.9	15.8	7.0	1.4
$V_{OC}$ (mV)	680	664	581	192
FF (%)	79.6	72.9	37.9	25.3
$j_{SC}$ (mA/cm <sup>2</sup> )	31.3	32.6	31.9	28.1

30 September 2023 04:29:08

x rays, especially of the O- $K_{\alpha}$  line, needs to be considered. For this purpose, the thickness of the TEM lamella was determined by the EDXS analysis of regions with a prior known O concentration. This is the case for the ZnO and (Zn,Mg)O layers where the O content is 50 at. %. The TEM lamella thickness was determined by adjusting the thickness for absorption correction such that the proper O stoichiometry was obtained. The determined thickness was then used for EDXS quantification of all elements with absorption correction.

High-resolution transmission electron microscopy (HRTEM) images and NBED patterns were acquired with a FEI Titan<sup>3</sup> 80–300 transmission electron microscope operated at 300 kV, which is equipped with an aberration corrector in the imaging lens system. The NBED patterns were recorded with a beam diameter of 7 nm and a convergence angle of 0.6 mrad for the incident electron beam. The diffracted intensity in the NBED patterns was azimuthally integrated ( $2\pi$  integral) and plotted as a function of the spatial frequency  $k$ . Structure analysis was performed using a whole diffraction-pattern fitting procedure to determine the position of each diffraction peak as a function of  $k$  after background subtraction by fitting Voigt functions to the profiles. It is demonstrated by Balzar and Popovic<sup>24</sup> that grain size and strain broadening of diffraction lines are well described by Voigt functions. To analyze the structure of possible crystalline phases, the resulting intensity profile was then compared with diffraction patterns calculated for possible phases (based on quantitative composition data) by using the JEMS program package.<sup>25,26</sup>

## RESULTS AND DISCUSSION

The bandgap energies of the as-grown and annealed Zn(O,S) layer from the poor-performing cell, respectively, were determined from the peak positions in the corresponding averaged ARER modulus spectra depicted in Fig. 1. Before annealing [Fig. 1(a)], a dominant resonance at 2.89 eV due to the  $E_g$  of the ternary Zn(O,S) buffer layer itself is detected. The high-energy contribution at

$\sim 3.2$  eV is an artifact caused by the small light intensity in this spectral region. After annealing at 250 °C [Fig. 1(b)], the  $E_g$  of Zn(O,S) slightly decreases from 2.89 to 2.84 eV, indicating a small change in stoichiometry. More importantly, the annealing process creates an additional strong resonance at 2.32 eV, hinting at the formation of a secondary phase with this  $E_g$ . However, it is noted that to a small degree, this secondary phase already seems to be present even before annealing [Fig. 1(a)], which could be an explanation for the poor device performance in the initial (as-grown) state.

To identify the chemical phase that contributes to the  $E_g$  of  $\sim 2.3$  eV in the annealed Zn(O,S) layer, STEM/EDXS was carried out. Figures 2(a) and 2(b) show a cross-sectional STEM-HAADF image of the CIGS/CBD-Zn(O,S)/(Zn,Mg)O/ZnO:Al interface region in the CIGS solar cell before thermal treatment and the corresponding quantified EDXS line profile of the area marked by a red arrow. In Fig. 2(a), the different layers can be well distinguished due to the composition sensitivity of the STEM-HAADF image contrast. An interface and corresponding layer roughness on the scale of a few 10 nm can be recognized. In Fig. 2(b), the concentration of each element is given as a function of the position indicated by the red arrow in Fig. 2(a). The composition gradients at the interfaces in Fig. 2(b) are broadened due to the small-scale interface roughness with respect to the TEM-specimen thickness of about 100 nm and the inclination of the electron beam with respect to the interfaces. The approximate positions of the inclined interfaces between adjacent layers are marked by dotted lines. The position of the CIGS/Zn(O,S) interface is located at the intersection of the Cu and the Zn concentration lines, the Zn(O,S)/(Zn,Mg)O interface at the intersection of the S and the Mg concentration lines, and the (Zn,Mg)O/ZnO:Al interface is defined at the point where the Mg concentration decreases to  $\sim 50\%$  of its maxima concentration. The Cu concentration in the CIGS absorber is a bit higher than the nominal value due to stray x rays that are generated because even the low-background TEM sample holder is not completely Cu-free. Due to absorption correction, the O content in the ZnO:Al

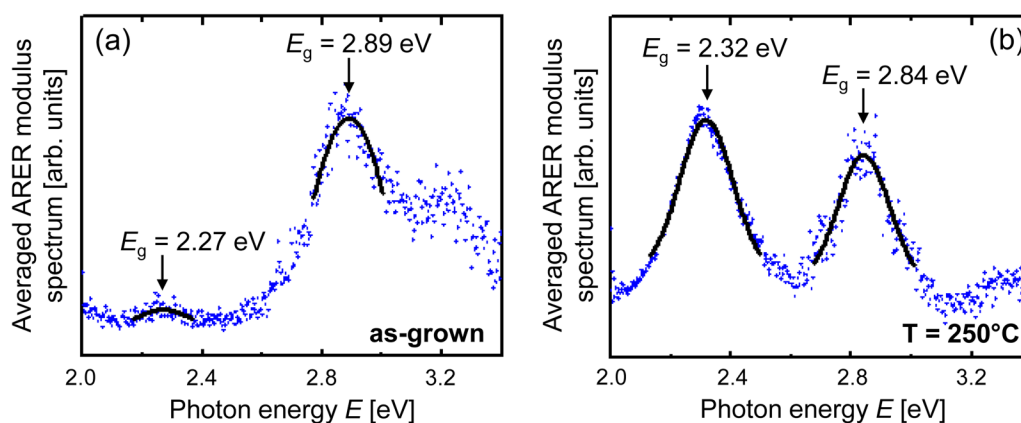


**FIG. 1.** Averaged ARER modulus spectra of the CBD-Zn(O,S) buffer layer in a complete CIGS solar cell with low power conversion efficiency (a) in an as-grown state and (b) after annealing at 250 °C. Local Gaussian fits (black lines) were used to estimate the peak positions corresponding to the  $E_g$  values of Zn(O,S) and the observed secondary phase, respectively.

30 September 2023 04:29:08

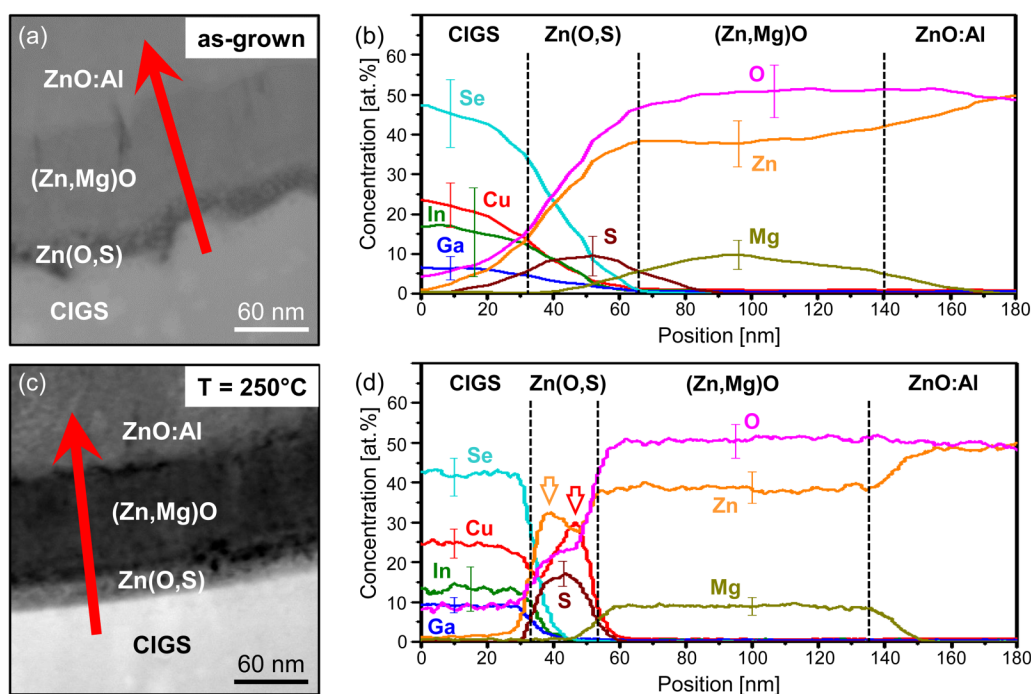


**FIG. 2.** Cross-sectional STEM-HAADF images of the CIGS/CBD-Zn(O,S)/(Zn,Mg)O/ZnO:Al interfacial region of the low-efficiency cell (a) in an as-grown state and (c) after annealing at 250 °C; (b) and (d) corresponding quantified EDXS line profiles for the elements Cu (red), In (green), Ga (blue), Se (turquoise), Zn (orange), O (pink), S (brown), and Mg (olive) as a function of position across the absorber/buffer/window layer region marked by a red arrow in (a) and (c).

(the low Al content of 1.6 at. % is ignored) and the (Zn,Mg)O layers amounts to 50 at. %, which is in agreement with the nominal value, indicating the reliability of the quantified EDXS analyses. Considering only the O and S content in the CBD-Zn(O,S) layer, the O concentration is always higher than the S content in this sample. In contrast to this, the chemical composition of similar Zn(O,S) layers was measured S-rich for layers deposited on top of different substrates such as glass/Mo or glass/CIGS without any further subsequent layers.<sup>16,27,28</sup> It seems that due to the deposition of the (Zn,Mg)O and ZnO:Al layers to fabricate the full device, there is a change in the  $[S]/([S] + [O])$  (SSO) ratio from S-rich to O-rich for the investigated sample. The other elements detected in the buffer layer, e.g., Se, Cu, In, Ga, and Mg, are artifacts due to the inclination of the interfaces with respect to the electron-beam direction. We note that the relatively high O concentration in the CIGS absorber is an artifact due to a surface oxidation of the TEM lamella.

Figures 2(c) and 2(d) show a STEM-HAADF image and a quantified EDXS line profile of the same region from the annealed CIGS solar cell. The interfaces in the region of Fig. 2(c) are less corrugated than in the region of Fig. 2(a), leading to abrupt contrast changes between the different layers. In addition, the composition gradients in Fig. 2(d) are steeper than in Fig. 2(b). However, this does not imply that the interface of the annealed sample is generally less corrugated than before annealing. A remarkable increase of the Cu concentration [red line in Fig. 2(d)] is observed close to the

Zn(O,S)/(Zn,Mg)O interface, marked by a red arrow, where S from Zn(O,S) and Mg from (Zn,Mg)O rather than Se, In, and Ga from CIGS are present, while the Zn concentration (orange line) is reduced. At the buffer/absorber interface, where S from Zn(O,S) and Se, In, and Ga from CIGS, rather than Mg from (Zn,Mg)O, are detected, the Zn concentration is enhanced, while the Cu concentration is lowered (cf. orange arrow), indicating the interdiffusion of Cu and Zn at the buffer/absorber interface. It was previously reported by Witte *et al.*<sup>16</sup> that post-annealing at 200 °C for 30 min leads to an in-diffusion of Zn from CBD-Zn(O,S) into CIGS, which is in agreement with our results. However, the Cu diffusion from CIGS into Zn(O,S) was not reported. These differences from our present results can be rationalized by the lower annealing temperature and higher SSO compared with our experimental conditions. In addition, Bär *et al.*<sup>29</sup> reported that a small amount of Cu was found to diffuse into the ZnS layer at the heterointerface between Se-free CuInS<sub>2</sub> and CBD-Zn(O,S)/ZnS, forming a Zn–Cu–S-like interlayer between the buffer and the absorber. They also observed a diffusion of Zn into the uppermost absorber region already during the chemical-bath deposition and this interdiffusion was enhanced by post-annealing at 200 °C for 5 min. Thus, the mechanism of this diffusion was interpreted as a CBD-induced and heat-treatment promoted Cu–Zn exchange at the buffer/absorber interface. In our work, the Cu–Zn interdiffusion was not observed at the interface between CIGS and Zn(O,S) grown at 80 °C by CBD but was detected after post-annealing the complete solar cell at

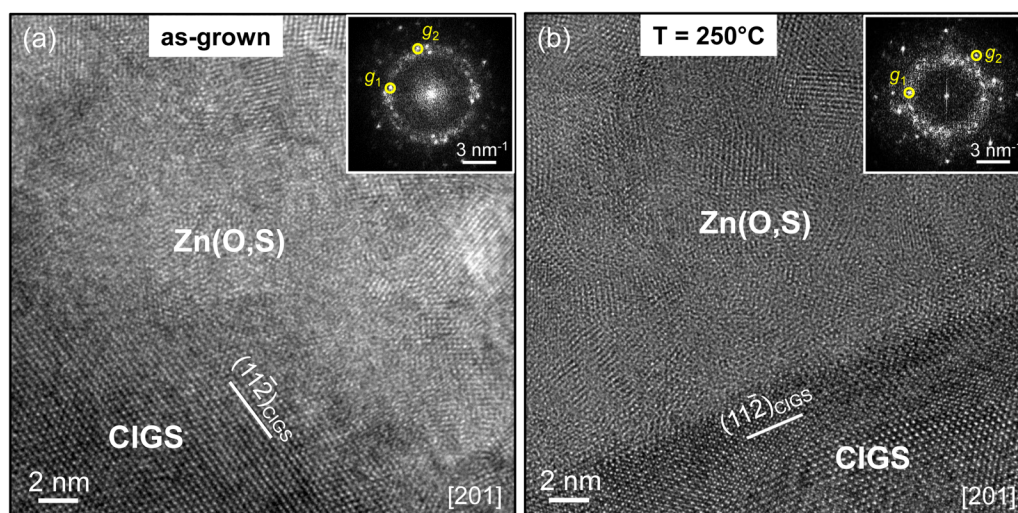


**FIG. 3.** High-resolution TEM images of the CIGS/CBD-Zn(O,S) interfacial region and corresponding two-dimensional Fourier transform (insets in upper right corners) of the Zn(O,S) buffer layer in the complete CIGS solar cell with low efficiency (a) in an as-grown state and (b) after annealing at 250 °C, recorded along the [201] zone axis of CIGS. The CIGS/Zn(O,S) interface is parallel to the (112) plane of CIGS in (b).

250 °C for 30 min. It seems that the Cu–Zn exchange depends not only on temperature but also on the composition of the absorber layer at the heterointerface. Moreover, Cu diffusion from CIGS into the buffer layer was also reported for the CIGS/CdS interface<sup>30</sup> and the CIGS/In<sub>2</sub>S<sub>3</sub> interface.<sup>31</sup> In combination with the ARER results shown in Fig. 1(b), the formation of a Cu-containing phase with an  $E_g$  of ~2.3 eV is supposed in the annealed CIGS cell with a Zn(O,S) buffer layer.

The crystallinity of the CBD-Zn(O,S) layer was investigated by HRTEM imaging as shown in Fig. 3. An HRTEM image of an interfacial region between CIGS and Zn(O,S) in the as-grown solar-cell device is presented in Fig. 3(a), which was recorded along the CIGS [201] zone axis. CIGS and the buffer can be well distinguished due to their different crystallinities. In contrast to the large CIGS grains, the Zn(O,S) layer contains nanocrystallites with random orientation, which is also observable in the two-dimensional Fourier transform of the buffer layer [the inset in Fig. 3(a)]. The reflections in the Fourier transform were evaluated to determine lattice-plane distances for the identification of crystal structures and (in combination with composition) phases. Assuming both ZnO and ZnS with the hexagonal wurtzite structure (cf. Table II for crystal structure data), the spatial frequency  $g_1 = 3.504 \text{ nm}^{-1}$  (with an error of  $\pm 0.1 \text{ nm}^{-1}$ ) fits either the (10 $\bar{1}$ 0) ZnO planes ( $3.553 \text{ nm}^{-1}$ ) or the (10 $\bar{1}$ 1) ZnS planes ( $3.417 \text{ nm}^{-1}$ ), and  $g_2 = 4.07 \text{ nm}^{-1}$  agrees well with the (10 $\bar{1}$ 1) ZnO planes ( $4.039 \text{ nm}^{-1}$ ). The reflections between them likely correspond to Zn(O,S) compounds. The other regions of the Zn(O,S)/CIGS interface were additionally studied, and the Zn(O,S) layer always exhibits a nanocrystalline structure, indicating that the nanocrystallinity of the Zn(O,S) does not depend on the orientation of the underlying CIGS grains. These results are consistent with those of our previous findings,<sup>21</sup> i.e., the as-grown CBD-Zn(O,S) layer contains a ternary

Zn(O,S) compound with a nanocrystalline structure. For comparison, Fig. 3(b) depicts an HRTEM image of a Zn(O,S)/CIGS interface in the annealed device that was also recorded along the CIGS [201] zone axis. The interface is clearly aligned parallel to the (11 $\bar{2}$ ) CIGS planes. The annealed Zn(O,S) layer also has a nanocrystalline structure indicating that annealing at 250 °C for 30 min does not significantly change the crystallinity of the Zn(O,S) buffer layer. The reflections of the corresponding Fourier transformation shown as an inset in Fig. 3(b) were also analyzed. For example,  $g_1 = 3.46 \text{ nm}^{-1}$  agrees with both the (10 $\bar{1}$ 0) ZnO planes and the (10 $\bar{1}$ 1) ZnS planes [similar to  $g_1 = 3.504 \text{ nm}^{-1}$  in Fig. 3(a)]. However,  $g_2 = 4.695 \text{ nm}^{-1}$  fits neither ZnO nor ZnS, which probably results from a Zn(O,S) phase or a Cu-containing phase, as indicated by the STEM/EDXS and ARER measurements. However, the number of relevant  $g$  values in Figs. 3(a) and 3(b) is not sufficient to precisely determine the phases in the buffer layer.

Different results were reported in the literature regarding the crystalline structure and composition of CBD-grown Zn(O,S) layers. Ahn *et al.*<sup>37</sup> have prepared CBD-Zn(O,S) layers in acidic and in alkaline solutions at 70 °C and 80 °C, respectively. X-ray photoelectron spectroscopy was performed to investigate the elemental composition according to the chemical bonding states of the Zn(O,S) thin films. In the acidic environment, mostly pure ZnS layers were deposited (i.e., no ZnO fraction was observed), while in the alkaline medium, the grown layers included amounts of oxygen exhibiting a composition of ZnO<sub>0.5</sub>S<sub>0.5</sub>. Additionally, the acidic grown ZnS layers showed a better crystallinity with larger grains than the alkaline grown Zn(O,S). After annealing ZnO<sub>0.5</sub>S<sub>0.5</sub> at 300 °C in vacuum, the S content increased without any change in the crystallinity, which is in agreement with our results. Gautron *et al.*<sup>38</sup> studied the microstructure of Zn(O,S) buffer layers on CIGS deposited by CBD. The CBD-Zn(O,S) layer with SSO = 0.6 exhibits

**TABLE II.** Bandgap energies  $E_g$  determined by ARER (marked with \*) or from the literature, corresponding  $x$  values, as well as  $a$  and  $c$  lattice parameters for wurtzite Zn(O,S) with different  $x$ , wurtzite CuS, cubic Cu<sub>2</sub>Se, and tetragonal Cu<sub>3</sub>Se<sub>2</sub>.

Compound	$E_g$ (eV)	Structure	$x$	$a$ (Å)	$c$ (Å)
ZnO	3.2	Wurtzite/P6 <sub>3</sub> mc <sup>32</sup>	0	3.2	5.2
ZnS	3.6	Wurtzite/P6 <sub>3</sub> mc <sup>33</sup>	1	3.8	6.3
Before thermal treatment					
Zn(O,S)	2.89*	Wurtzite/P6 <sub>3</sub> mc <sup>7</sup>	0.72	3.6	5.9
			0.15	3.3	5.4
After thermal treatment					
Zn(O,S)	2.84*	Wurtzite/P6 <sub>3</sub> mc <sup>7</sup>	0.7	3.6	5.9
			0.17	3.3	5.4
CuS	2.36	Wurtzite/P6 <sub>3</sub> mc <sup>34</sup>		3.8	16.3
Cu <sub>2</sub> Se	2.23	Cubic/Fm-3 m <sup>35</sup>		5.7	
Cu <sub>3</sub> Se <sub>2</sub>	2.37	Tetragonal/P-421 m <sup>36</sup>		6.4	4.3

an extra thin ZnS layer at the Zn(O,S)/CIGS interface showing high crystallinity and a well-defined orientation relationship with CIGS, i.e., cubic ZnS (111) planes or hexagonal ZnS (0002) planes parallel to the tetragonal CIGS (112) planes. Considering that in our work the deposition temperature and the film thickness of the CBD-Zn(O,S) layer are similar to those in Ref. 38, the absence of a thin crystalline ZnS layer at the buffer/absorber interface and the existence of a ternary Zn(O,S) compound could be related to the smaller SSO value, which could be the result of different sputtering conditions for the subsequent high-resistive and window layers. We suggest that the nanocrystalline CBD-Zn(O,S) layer in our work can be explained by a cluster-by-cluster growth during CBD according to Ref. 38 as a dominant growth mechanism leading to the nanocrystalline structure.

To obtain more information on the crystal structure in our nanocrystalline CBD-Zn(O,S) buffer layers, NBED patterns were considered. Figures 4(a) and 4(c) show NBED patterns of the Zn

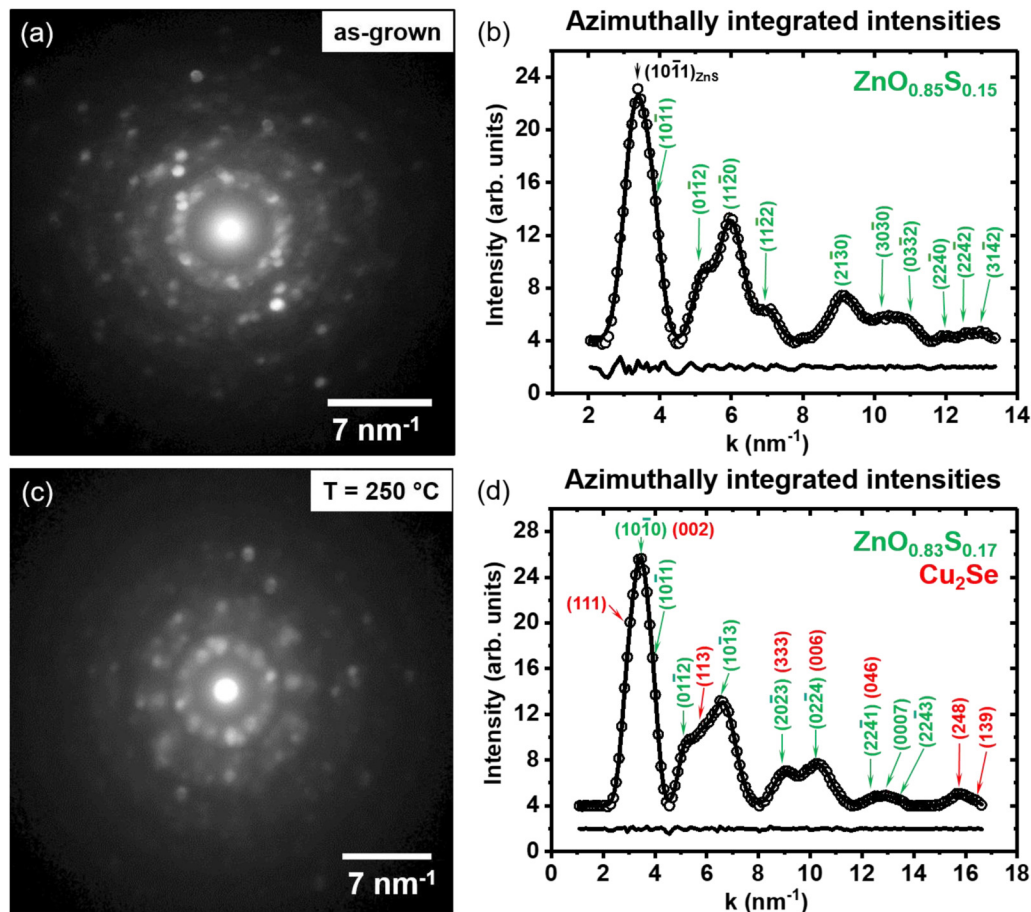


**FIG. 4.** NBED pattern of the CBD-Zn(O,S) layer of the low-efficiency cell (a) in an as-grown state and (c) after annealing at 250 °C; (b) and (d) azimuthally integrated intensity profiles of the NBED patterns in (a) and (c).

(O,S) buffer layer before and after thermal treatment, respectively. The zero-order beam of the unscattered electrons is located in the center. Numerous Bragg reflections arranged in rings are visible at different spatial frequencies, which are characteristic of the crystal structure of the phases present in the buffer layer. Figures 4(b) and 4(d) show the corresponding intensity profiles as a function of the spatial frequency  $k$  that were obtained by an azimuthal integration of the NBED patterns. For the evaluation of the intensity profiles, we assume that Zn(O,S) is present in the hexagonal wurtzite structure (space group  $P6_3mc$ )<sup>7</sup> with lattice parameters that depend on the SSO ratio denoted as  $x$  in the following. As a first approach to determine the SSO, we use the  $E_g$  of 2.89 eV obtained by ARER and extract  $x$  by exploiting the composition dependence of the bandgap energy of Zn(O,S)  $E_{g,Zn(O,S)}$  given by

$$E_{g,Zn(O,S)}(x) = x^*E_{g,ZnS} + (1-x)^*E_{g,ZnO} - b^*(1-x)^*x, \quad (1)$$

where  $E_{g,ZnS}$  and  $E_{g,ZnO}$  are the bandgap energies of ZnS (3.6 eV) and of ZnO (3.2 eV) and  $b = 3.0$  eV is the bowing parameter.<sup>7</sup>  $E_{g,Zn(O,S)} = 2.89$  eV yields  $x$  values of 0.72 or 0.15. For the determination of the  $a$  and  $c$  lattice parameters of wurtzite Zn(O,S), we assume that the lattice parameters depend linearly on  $x$  between the values of the binary compounds (cf. Table II for the lattice parameters of ZnO and ZnS).<sup>7</sup> The evaluated  $a$  and  $c$  lattice parameters are also given in Table II. The fit of the intensity profile in Fig. 4(b) suggests that  $ZnO_{0.85}S_{0.15}$  is present. This composition is also consistent with that of the STEM/EDXS results in Fig. 2(b), which shows a high O content. We note that the most intense peak of the profile can be fitted only with the (10 $\bar{1}$ 1) ZnS reflection, but the  $E_g$  of 3.6 eV for pure ZnS is beyond the detection limit of our ARER setup.

After thermal treatment, the measured  $E_g$  of 2.84 eV [cf. Fig. 1(b)] suggests  $x$  values of 0.17 or 0.7 with the  $a$  and  $c$  lattice parameters given in Table II. The fit of the intensity profile in Fig. 4(d) suggests that  $ZnO_{0.83}S_{0.17}$  is present. An additional  $E_g$  of 2.32 eV detected by ARER indicates the presence of a secondary phase. Considering the annealing-induced Cu diffusion from CIGS into Zn(O,S) [cf. Fig. 2(d)], the secondary phase is most likely a Cu-containing phase, e.g., CuS, Cu<sub>2</sub>Se, or Cu<sub>3</sub>Se<sub>2</sub> (cf. Table II for  $E_g$  and structure data). In the region where the NBED pattern of Fig. 4(d) was considered, Cu<sub>2</sub>Se fits the profile better than the other phases. In addition to the presence of Cu<sub>2</sub>Se-specific (248) and (139) reflections at large  $k$  values, we obtain a very good fit for  $2 \text{ nm}^{-1} \leq k \leq 8.3 \text{ nm}^{-1}$  ( $R^2 = 0.999$ ) by considering the (111), (002), and (113) Cu<sub>2</sub>Se reflections. The overall  $k$  range is smaller in Fig. 4(b) for the as-grown sample because the NBED pattern was considered at a higher magnification and did not allow us to detect the high-index Cu<sub>2</sub>Se reflections. However, a high-fit quality for the as-grown sample ( $R^2 = 0.997$ ) was obtained in the  $k$  range  $2 \text{ nm}^{-1} \leq k \leq 8.5 \text{ nm}^{-1}$  without the (111), (002), and (113) Cu<sub>2</sub>Se reflections. This demonstrates that Cu<sub>2</sub>Se is, indeed, formed during annealing. In another analyzed region (not shown here), hexagonal CuS yields the best fit. CuS was detected only in one local region, indicating that the volume fraction of CuS is small. This observation indicates the coexistence of Cu<sub>2</sub>Se, CuS, and Zn(O,S) with  $x \approx 0.17$ . Nevertheless, other phases cannot be completely excluded due to

the small volume analyzed by NBED and the chemical inhomogeneity of the annealed CBD-Zn(O,S) layer.

## CONCLUSIONS

The bandgap energies and microstructure of solution-grown Zn(O,S) as the buffer layer in complete CIGS solar cells were studied. The investigations were performed on as-grown and post-annealed (250 °C in air) devices with a low power conversion efficiency of 7% in the as-grown state to shed more light on the possible origins of the poor device performance. In the as-grown state, bandgap measurements on the Zn(O,S)/CIGS interface by ARER indicate the formation of the ternary compound Zn(O,S) with  $E_g \sim 2.89$  eV. After annealing, the  $E_g$  of Zn(O,S) slightly decreased, and a second bandgap energy  $E_g$  of  $\sim 2.3$  eV was clearly detected, suggesting the formation of an additional phase. The microchemistry of the interfacial region between CIGS and CBD-Zn(O,S) as well as the buffer itself was analyzed by combined STEM/EDXS. Cu–Zn interdiffusion at the interface was detected, which was induced and promoted by the post-annealing, probably leading to a Cu-containing phase. HRTEM imaging of the buffer/absorber interface showed a nanocrystalline structure of the Zn(O,S) buffer layer, which was independent of the orientation of the underlying CIGS grains and which hardly changed by post-annealing. According to NBED and the corresponding azimuthally integrated intensity profile, the Cu-containing secondary phase is most likely a mixture of cubic Cu<sub>2</sub>Se (major) and hexagonal wurtzite CuS (minor), which could be one possible explanation for the very low efficiency and low fill factor due to severe shunting caused by the high annealing temperature. We must acknowledge that only a small volume can be investigated by TEM and, using only TEM, other phases cannot be excluded. However, information from a larger region is obtained by ARER with a spot size of 1–2 mm<sup>2</sup>, and the correlation of the bandgap energies with the microstructure data indicates that the detected phases occur not only in the regions analyzed by TEM. Our studies, therefore, also demonstrate that a combination of ARER and TEM is a powerful tool to determine the complex chemical phase formation in complete CIGS thin-film solar cells on the submicrometer scale, especially at interfaces like the important p–n junction, which has a direct impact on thin-film solar-cell performance.

## ACKNOWLEDGMENTS

We acknowledge the funding by the German Federal Ministry for Economic Affairs and Climate Action (BMWK) within the EFFCIS-II project under Contract No. 03EE1059A (ZSW) and Contract No. 03EE1059E (KIT). We also acknowledge the CIGS team at ZSW for solar-cell fabrication. Furthermore, Professor H. Kalt at the Institute of Applied Physics (KIT) is acknowledged for fruitful discussions.

## AUTHOR DECLARATIONS

### Conflict of Interest

The authors have no conflicts to disclose.



### Author Contributions

**Xiaowei Jin:** Conceptualization (lead); Data curation (lead); Formal analysis (lead); Investigation (lead); Methodology (lead); Writing – original draft (lead); Writing – review & editing (lead). **Reinhard Schneider:** Funding acquisition (lead); Investigation (equal); Methodology (equal); Project administration (lead); Writing – review & editing (equal). **Radian Popescu:** Methodology (equal); Writing – review & editing (equal). **Jasmin Seeger:** Conceptualization (equal); Investigation (equal); Methodology (equal); Writing – review & editing (supporting). **Jonas Grutke:** Investigation (supporting); Methodology (supporting); Writing – review & editing (supporting). **Benedikt Zerulla:** Investigation (supporting); Methodology (supporting); Writing – review & editing (supporting). **Michael Hetterich:** Funding acquisition (equal); Investigation (equal); Methodology (equal); Project administration (lead); Writing – review & editing (equal). **Dimitrios Hariskos:** Investigation (equal); Methodology (equal); Writing – review & editing (equal). **Wolfram Witte:** Funding acquisition (lead); Investigation (equal); Methodology (equal); Project administration (lead); Writing – review & editing (equal). **Michael Powalla:** Funding acquisition (lead); Project administration (lead); Writing – review & editing (supporting). **Dagmar Gerthsen:** Conceptualization (equal); Funding acquisition (lead); Investigation (equal); Methodology (equal); Project administration (lead); Supervision (lead); Writing – review & editing (equal).

### DATA AVAILABILITY

The data that support the findings of this study are available within the article.

### REFERENCES

- <sup>1</sup>M. Nakamura, K. Yamaguchi, K. Yoshinori, Y. Yasaki, T. Kato, and H. Sugimoto, *IEEE J. Photovolt.* **9**, 1863 (2019).
- <sup>2</sup>A. Kowsar, M. Rahaman, M. S. Islam, A. Y. Imam, S. C. Debnath, M. Sultana, M. A. Hoque, A. Sharmin, Z. H. Mahmood, and S. F. U. Farhad, *Int. J. Renew. Energy Res.* **9**, 579 (2019).
- <sup>3</sup>J. Ramanujam and U. P. Singh, *Energy Environ. Sci.* **10**, 1306 (2017).
- <sup>4</sup>T. Feurer, P. Reinhard, E. Avancini, B. Bissig, J. Löckinger, P. Fuchs, R. Carron, T. P. Weiss, J. Perrenoud, S. Stutterheim, S. Buecheler, and A. N. Tiwari, *Prog. Photovolt. Res. Appl.* **25**, 645 (2017).
- <sup>5</sup>P. Jackson, R. Wuerz, D. Hariskos, E. Lotter, W. Witte, and M. Powalla, *Phys. Status Solidi RRL* **10**, 583 (2016).
- <sup>6</sup>M. Cardona, M. Weinstein, and G. A. Wolff, *Phys. Rev.* **140**, A633 (1965).
- <sup>7</sup>B. K. Meyer, A. Polity, B. Farangis, Y. He, D. Hasselkamp, T. Krämer, and C. Wang, *Appl. Phys. Lett.* **85**, 4929 (2004).
- <sup>8</sup>K. S. Gour, R. Parmar, R. Kumar, and V. N. Singh, *J. Nanosci. Nanotechnol.* **20**, 3622 (2020).
- <sup>9</sup>J. H. Choi, S. H. Jung, and C. W. Chung, *J. Nanosci. Nanotechnol.* **16**, 5378 (2016).
- <sup>10</sup>M. Buffière, S. Harel, C. Guillot-Deudon, L. Arzel, N. Barreau, and J. Kessler, *Phys. Status Solidi A* **212**, 282 (2015).
- <sup>11</sup>C. Platzer-Björkman, T. Törndahl, D. Abou-Ras, J. Malmström, J. Kessler, and L. Stolt, *J. Appl. Phys.* **100**, 044506 (2006).
- <sup>12</sup>A. Ennaoui, M. Bär, J. Klaer, T. Kropp, R. Sáez-Araoz, and M. C. Lux-Steiner, *Prog. Photovolt. Res. Appl.* **14**, 499 (2006).
- <sup>13</sup>C. Chen, S. Cheng, H. Zhang, H. Zhou, and H. Jia, *Cryst. Res. Technol.* **51**, 354 (2016).
- <sup>14</sup>J. Seeger, B. Zerulla, J. Grutke, W. Witte, D. Hariskos, O. Kiowski, H. Kalt, and M. Hetterich, *2019 IEEE 46th Photovoltaic Specialists Conference (PVSC) (IEEE, 2019)*, p. 0949.
- <sup>15</sup>J. Seeger, J. Grutke, N. Weber, S. Schützhoff, X. Jin, R. Schneider, D. Gerthsen, W. Witte, D. Hariskos, O. Kiowski, M. Schweiger, H. Kalt, and M. Hetterich, *Appl. Phys. Lett.* **115**, 263901 (2019).
- <sup>16</sup>W. Witte, D. Hariskos, A. Eicke, R. Menner, O. Kiowski, and M. Powalla, *Thin Solid Films* **535**, 180 (2013).
- <sup>17</sup>S. Lee, E. S. Lee, T. Y. Kim, J. S. Cho, Y. J. Eo, J. H. Yun, and A. Cho, *Sol. Energy Mater. Sol. Cells* **141**, 299 (2015).
- <sup>18</sup>D. H. Shin, S. T. Kim, J. H. Kim, H. J. Kang, B. T. Ahn, and H. Kwon, *ACS Appl. Mater. Interfaces* **5**, 12921 (2013).
- <sup>19</sup>T. Kobayashi, T. Kumazawa, Z. Jehl Li Kao, and T. Nakada, *Sol. Energy Mater. Sol. Cells* **123**, 197 (2014).
- <sup>20</sup>G. Voorwinden, R. Kniese, P. Jackson, and M. Powalla, *22nd European Photovoltaic Solar Energy Conference (WIP-Renewable Energies, 2007)*, p. 2115.
- <sup>21</sup>X. Jin, R. Popescu, A. Pasha, R. Schneider, D. Hariskos, W. Witte, M. Powalla, and D. Gerthsen, *Thin Solid Films* **671**, 133 (2019).
- <sup>22</sup>D. Hariskos, P. Jackson, W. Hempel, S. Paetel, S. Spiering, R. Menner, W. Wischmann, and M. Powalla, *IEEE J. Photovolt.* **6**, 1321 (2016).
- <sup>23</sup>G. Cliff and G. W. Lorimer, *J. Microsc.* **103**, 203 (1975).
- <sup>24</sup>D. Balzar and S. Popović, *J. Appl. Cryst.* **29**, 16 (1996).
- <sup>25</sup>P. A. Stadelmann, *Ultramicroscopy* **21**, 131 (1987).
- <sup>26</sup>X. Jin, R. Schneider, R. Popescu, D. Hariskos, W. Witte, M. Powalla, and D. Gerthsen, *Semicond. Sci. Technol.* **35**, 034001 (2020).
- <sup>27</sup>A. Eicke, T. Ciba, D. Hariskos, R. Menner, C. Tschamber, and W. Witte, *Surf. Interface Anal.* **45**, 1811 (2013).
- <sup>28</sup>T. Adler, M. Botros, W. Witte, D. Hariskos, R. Menner, M. Powalla, and A. Klein, *Phys. Status Solidi A* **211**, 1972 (2014).
- <sup>29</sup>M. Bär, A. Ennaoui, J. Klaer, T. Kropp, R. Sáez-Araoz, S. Lehmann, A. Grimm, I. Lauer, C. Loreck, S. Sokoll, H. W. Schock, C. H. Fischer, M. C. Lux-Steiner, and C. Jung, *J. Appl. Phys.* **100**, 064911 (2006).
- <sup>30</sup>P. M. P. Salome, R. Ribeiro-Andrade, J. P. Teixeira, J. Keller, T. Törndahl, N. Nicoara, M. Edoff, J. C. Gonzalez, J. P. Leitao, and S. Sadewasser, *IEEE J. Photovolt.* **7**, 858 (2017).
- <sup>31</sup>S. Spiering, A. Eicke, D. Hariskos, M. Powalla, N. Naghavi, and D. Lincot, *Thin Solid Films* **451–452**, 562 (2004).
- <sup>32</sup>S. C. Abrahams and J. L. Bernstein, *Acta Cryst.* **25**, 1233 (1969).
- <sup>33</sup>E. H. Kisi and M. M. Elcombe, *Acta Cryst.* **C45**, 1867 (1989).
- <sup>34</sup>H. J. Gotsis, A. C. Barnes, and P. Strange, *J. Phys.: Condens. Matter.* **4**, 10461 (1992).
- <sup>35</sup>K. Yamamoto and S. Kashida, *J. Solid State Chem.* **93**, 202 (1991).
- <sup>36</sup>R. D. Heyding and R. M. Murray, *Can. J. Chem.* **54**, 841 (1976).
- <sup>37</sup>K. Ahn, J. H. Jeon, S. Y. Jeong, J. M. Kim, H. S. Ahn, J. P. Kim, E. D. Jeong, and C. R. Cho, *Curr. Appl. Phys.* **12**, 1465 (2012).
- <sup>38</sup>E. Gautron, M. Buffière, S. Harel, L. Assmann, L. Arzel, L. Brohan, J. Kessler, and N. Barreau, *Thin Solid Films* **535**, 175 (2013).